Chapter 2

The MPIA Wide Field EROs Survey

This chapter introduces a wide-field near-infrared survey, established 1997 as completion to the large optical data set of the *High-Redshift Supernova Search Project*. We will describe the available data and the data reduction pipeline. A large fraction of this chapter deals with the calibration of the optical data, especially with the limitations of the initially used method. Unfortunately, the problem was not encountered until we could compare the optical photometry with the results of the Sloan Digital Sky Survey.

Originally dedicated to the search for old, field brown dwarfs (Herbst et al. 1999), the optical and near-infrared wide-field survey of the Max-Planck Institute for Astronomy proved to be very suitable for the detection of extremely red galaxies. The combination of R and J-band data facilitates the detection of a small, distinct sub-sample of the EROs population, avoiding the difficulties with classification. A detailed description of the colour classification follows in chapter 3.

The survey consists of 79 single fields, each covering approximately 15 $'\times$ 15$'$. At redshift z=1, the co-moving length of one field is approximately 5000 h^{-1}Mpc, i.e. large compared to the correlation length of r$_o \sim$ 7 h^{-1} Mpc. In total the fields represent $\sim$ 4.64 deg^2, observed both in R- and J-band and it is the largest ERO survey to date.
The results of previous studies shown a wide scattering in the surface density of EROs, which can be the result of cosmic variance, colour selection effects or different survey depths. Some of those surveys cover relatively small, connected areas (e.g. Barger et al. 1999, Cimatti et al. 2002a) and are therefor more sensitive to cosmic variance, especially considering the strong clustering seen by Daddi et al. (2000) and Roche et al. (2002). In order to reduce the effect of field-to-field variations, our single survey fields are widely spread over an equatorial stripe (Figure 2.1), allowing follow-up observations with telescopes in both the northern and southern hemisphere. The coordinates of all survey fields appear in Appendix B. To reduce the number of red stellar objects, e.g. low mass stars, we selected the fields at higher galactic latitudes, i.e 22$^o \leq$|b|$\leq$ 60°.
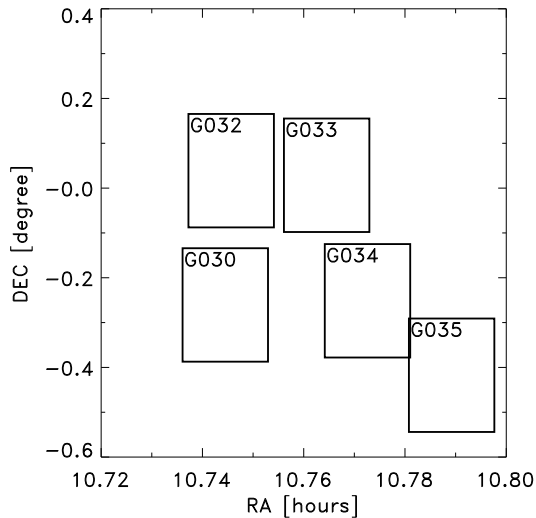
Figure 2.1: Example of the spatial distribution of the survey fields. Some fields might almost overlap, while others are isolated. For coordinates, see Appendix B.

2.1   Optical data

The R-band observations were taken independently as part of the *High-z Supernova Search Team Cosmology Project* with the 4.0 m Blanco telescope at the Cerro Tololo Inter-American Observatory (CTIO) (Schmidt et al. 1998). The data were obtained during runs in 1994 to 1996. The Prime Focus CCD Direct camera (PFCCD) was equipped with a 2048x2048 pixel array with 0.40 arcsec/pixel.

In order to use the optical data, we had to overcome two difficulties:

1. no standard star observations were available,

2. the total integration times range from 600 to 2820 seconds, resulting in different depth, and hence different limiting magnitudes, for each field.

2.1.1   Zero-point calibration

When we started to use these R-band data as basis for our survey, we were aware that we would need an alternative method to the commonly used calibration with standard stars. A promising approach seemed to be the calibration using an analytical expression for the **G**alaxy **N**umber **C**ount-**M**agnitude **R**elation (GNC-MR)(section 2.1.1.1).

However, with the second data release of the Sloan Digital Sky Survey (SDSS), we had the possibility to test the accuracy of this new method against the established photometry of SDSS. To do so, we compared the R-band photometry, based on the GNC-MR, of several stars (N>50) with their SDSS magnitudes.

The following sections will describe both methods and draw some conclusions in respect to the applicability of GNC-MR.

2.1.1.1 Galaxy number counts - The Metcalfe method

This method is based on work by Metcalfe et al. (1991), who looked at the B- and R-band galaxy number count-magnitude relations of 12 independent fields for $19^{mag} < R_{CCD} < 23.5^{mag}$. This method was not designed for zero-point magnitude calibrations, and we will see its limitations later on. (The zero-point magnitude is the equivalent to 1 detected photon per second and depends on the instrument as well as the observation site, airmass etc.
All objects classified as galaxies from the source catalogue were plotted on histograms with $\Delta R = 0.5 \ ^{mag}$ bins. The number counts were then normalised to 1 deg^2. The logarithmic distribution can be fitted by a power law of the form (2.1):

$$log \ N_{gal} \quad = \quad (0.373 \pm 0.01) \ R_{CCD} \ - \ (4.52 \pm 0.21) \ for \ 20^{mag} \ < \ R \ < \ 23^{mag} \quad (2.1)$$

$$log \ N_{gal} \quad = \quad 0.373 \ (R_{CCD} + \Delta R) \ - \ 4.52 \ for \ 20^{mag} \ < \ R \ < \ 23^{mag} \quad (2.2)$$

The objects were first detected using a randomly selected zero-point magnitude (ZPM) of 30.8. As can be seen from Figure 2.2, their number count distribution does not agree with the expression in equation 2.1. Even though the galaxy number count-magnitude relation is valid for $20^{mag} < R < 23^{mag}$, the faintest bins suffer a certain degree of incompleteness, which has been accepted in terms of a lower faint end limit, e.g. $R_{faint} = 22.5^{mag}$.
Nevertheless, we can obtain the necessary correction to the ZPM by fitting equation 2.2 to the galaxy number counts. This corrected zero-point was then used as input-parameter for SEXTRACTOR 2.2.2 (see chapter 2.3).

Figure 2.2 shows the result of this procedure for one of our survey fields. After the zero-point correction, both the slope and magnitude of the distribution are described well by equation 2.1.

While equation 2.1 describes the galaxy number count distribution well for both our optical data and for the fields of Metcalfe et al (1991), we took the opportunity to confirm these zero-points by comparing the R-band photometry with the results of the just published SDSS. Correct photometry is essential for a colour based galaxy selection, and this method has not been used for zero-point calibration before.

2.1.1.2 Cross check against the SDSS catalogue

With the recent publication of the second data release from the Sloan Digital Sky Survey, approximately 50% of our fields could be checked for consistency of the R-band magnitudes. Here, we have limited the cross check to point-like sources and with an R-band magnitude fainter than 16.7^{mag}. (This limit is based on the photometry using the zero-point from the galaxy number count approach.) If the Metcalfe technique works, there should be no difference between the magnitudes, except statistical scattering.
Because the SDSS R-filter has different transmission characteristics to the Cousins filter used with PFCCD, we had to convert the SDSS magnitudes into R_{Vega} magnitudes. The transformation equations (eq. 2.3) were derived from $u'g'r'i'z'$ photometry of 158 standard stars. The uncertainty in the mean calibrated magnitudes for any given standard star should be less than 1% in g' and r', resulting in a error of less than 0.02 mag in $g' - r'$ (Smith et al. 2002).
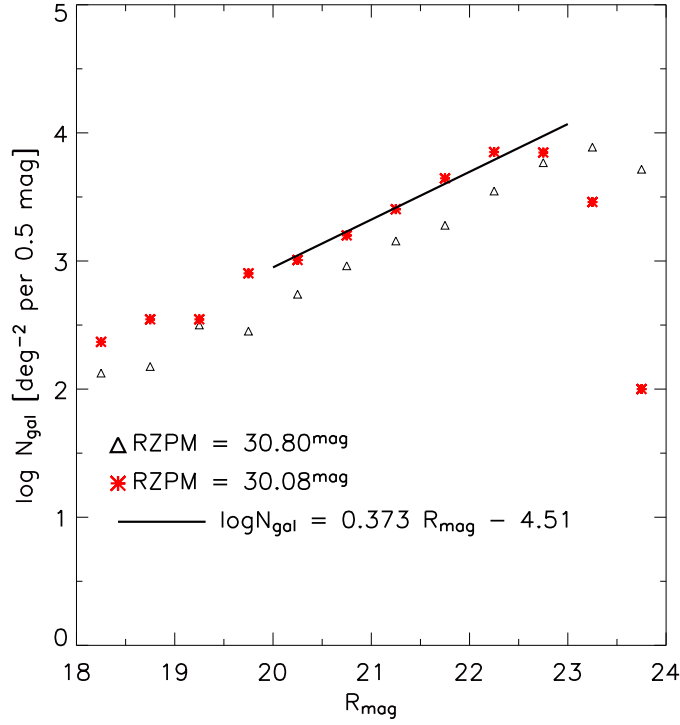
Figure 2.2: Differential galaxy number counts per 0.5^{mag} bin for a randomly selected survey field. Using equation 2.2, we can correct the zero-point to 30.08^{mag}. The line shows the agreement between the power law and the number count distribution after correcting the zero point magnitude (red symbols).

$$
\begin{aligned}
V &= g' - 0.55\ (g' - r') - 0.03 \\
V - R &= 0.59\ (g' - r') + 0.11 \\
R &= -0.14\ g' + 1.14\ r' + 0.14
\end{aligned}
\tag{2.3}
$$

Figure 2.3 shows the result for one of our fields, which shows a distinct offset between the zero-point derived from the galaxy number counts and the converted SDSS R-band magnitudes.

We cross checked all 79 fields against SDSS, producing the offsets shown in Figure 2.4. The offset distribution for all survey fields has a maximum at R_{CTIO}-$R_{SDSS} \approx 0.52^{mag}$ (see Figure 2.4), which is well above the error of ± 0.21 (eq. 2.1) given by Metcalfe et al (1991). The offset always has the same sign (Figure 2.4), i.e. the zero-points obtained with the Metcalfe method are always too faint, which is a serious problem for any R-J based colour selection. The offset can be calculated from a linear relation between both magnitudes, described by $R_{CTIO} = R_{SDSS} + \Delta R$.

The first step in finding the reason for the zero-point offset ΔR_{ZP} is testing whether or not there is a relation between the magnitude offset and the following parameters:
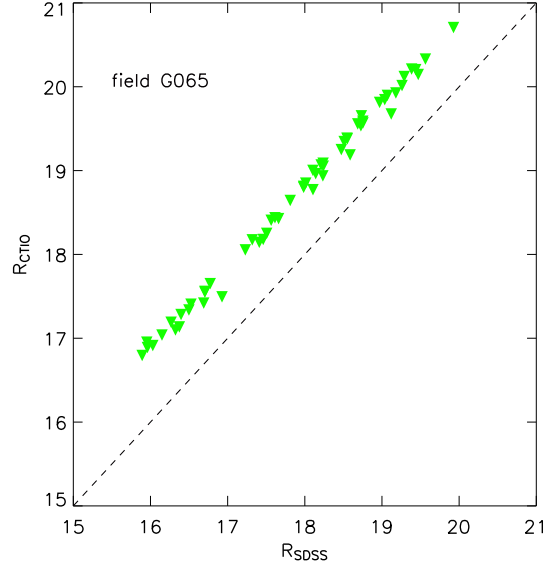
Figure 2.3: Comparison between the R-band magnitudes for one selected field. R_{CTIO} shows the R magnitudes, based on zero-points derived from the galaxy number count-magnitude relation (eq. 2.1). The SDSS magnitudes were calculated with equation 2.3.
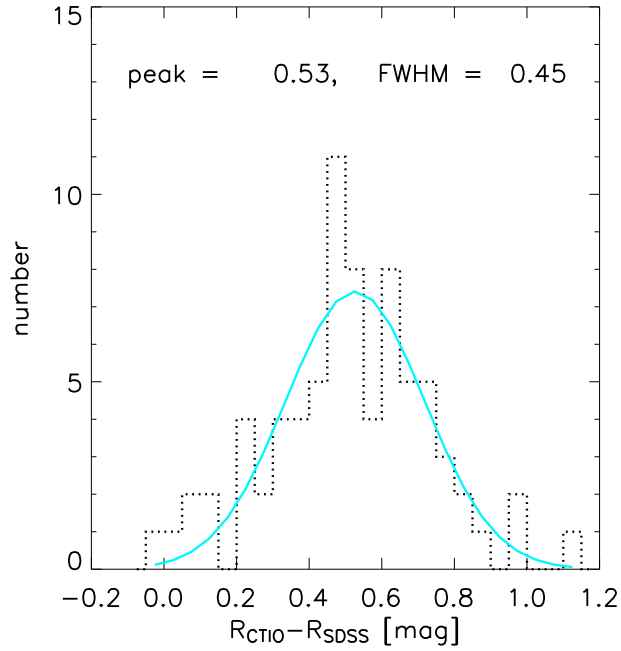

Figure 2.4: The distribution of the zero-point offsets shows a distinct peak at 0.52^{mag}. This large mean offset is not simply explained by the accuracy of the method (see chapter 2.1.1.1), for which we would assume a scattering around R_{CTIO}-$R_{SDSS} \sim 0$.

- position of a source on the detector

- surface density of galaxies per survey field (normalised to $1\deg^2$),

- star-galaxy classification based on stellarity index,

- galactic coordinates

The first parameter was checked to ensure that not fringes or residuals from the data reduction are responsible for eventual differences in the photometry (left panel in Figure 2.5). The remaining three factors influence either the galaxy number counts directly (e.g. presence of a galaxy cluster), or affect the assignment of a galaxy to a certain magnitude bin due to dimming or reddening (e.g. galactic extinction).
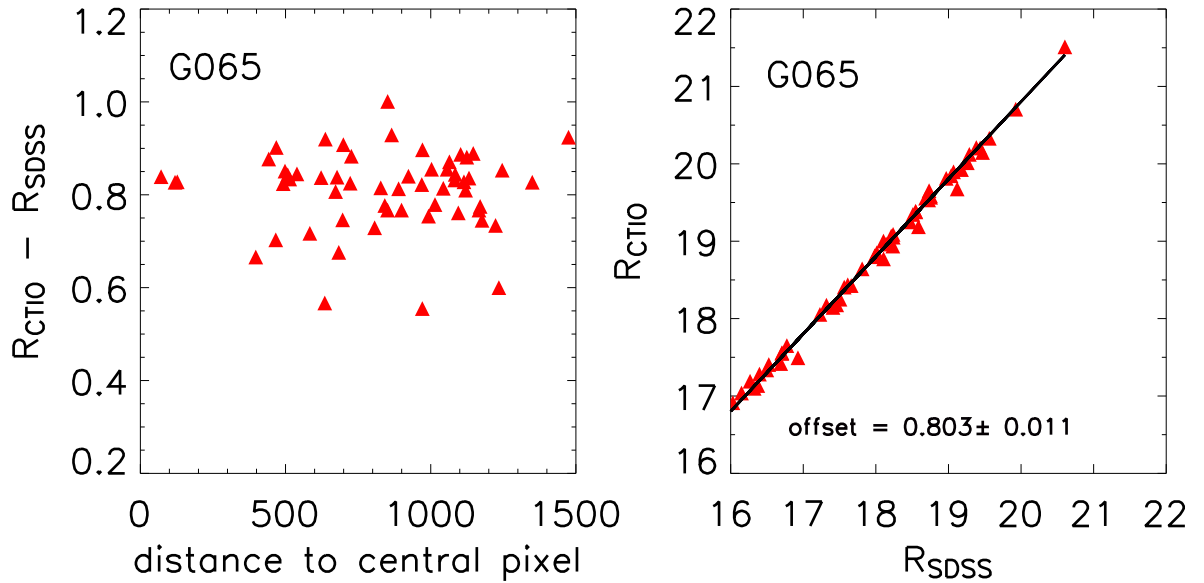

Figure 2.5: The left panel shows the dependence of the magnitude offset R_{CTIO}-R_{SDSS} on the distance to the central pixel. The offset between both magnitudes is obtained from a linear fit, whit the slope kept constant at 1, as we would expect for a linear detector (right panel).

2.1.1.3 Surface density of galaxies

A crucial influence on the R-band galaxy number-counts may be the presence of galaxy clusters in the field, as seen in Figure 2.6, which is adopted from Metcalfe et al. 1991. A rich cluster almost doubles their count at $R \approx 21^{mag}$ compared to any other field. Excluding this field reduces the mean count by approximately 10 per cent (Metcalfe et al. 1991).

The only parameter in in eq. 2.2 which can influence the calculation of the zero-point are the galaxy number counts. In Figure 2.7 we have plotted the zero-point offsets versus galaxy surface density. While we found a relatively weak correlation between the offset and the surface density of galaxies with the whole range of magnitudes, there is a tighter correlation to the surface density of galaxies with $23 \leq R \leq 23$. However, This supports the assumption that the total number of galaxies per square degree is not the major factor for the difference between R_{CTIO} and R_{SDSS} (in the text we use ΔRM when we refer to R_{CTIO} and R_{SDSS}).
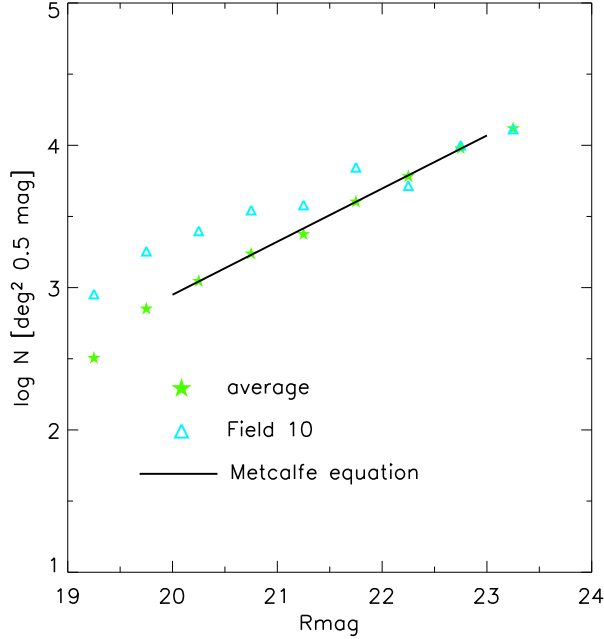

Figure 2.6: Differential galaxy number counts per 0.5^{mag} found by Metcalfe et al (Note that the values were taken from the figure 9 in Metcalfe et al (1991). The green symbols show the number counts averaged over all 14 R-band frames, the blue symbols show the result for field 10, which contains a distant rich cluster. The line represents equation 2.1.

Each of our survey fields covers about 10 times as much sky as was available to Metcalfe et al. (1991). To ensure that the much larger fields of our survey do not contain several rich galaxy clusters, which could limit the application of the power law fit, we looked at the spatial distribution of all galaxy detections in the fields (left panel Figure 2.7. We could detect only a weak dependence of the magnitude offset from the total number of galaxies, there is a clear correlation between the ΔRM and the number of galaxies with $20 \leq R \leq 23$ (right panel Figure 2.7). It also implies that the surface density of galaxies in this magnitude range is to
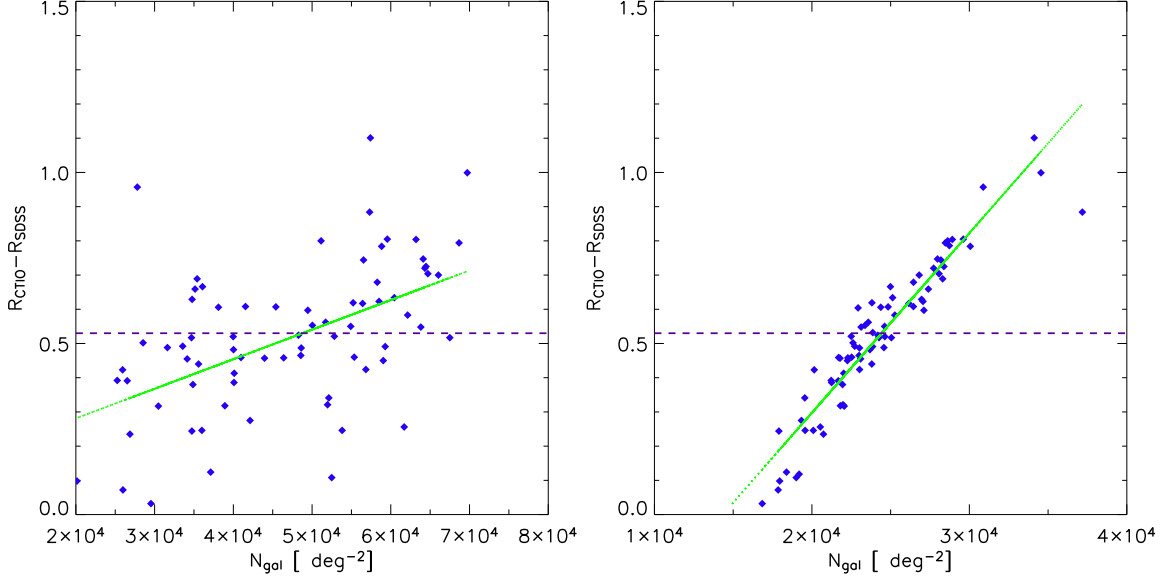
high for all our fields.

Figure 2.7: The offset between our R-band magnitudes and SDSS magnitudes as function of the total number of galaxies per square degree (left panel) and as function of the number of galaxies with $20 \leq R \leq 23$. The dashed line indicates the mean offset, derived from the peak position of an Gaussian distribution (see Figure 2.4).

Could we use a smaller fraction of each survey field to determine the correct zero-point? To answer this question, we examined on of our fields more carefully. Field G030 (for naming, coordinates and other parameters see Appendix B), has a magnitude offset of $\Delta RM \approx 0.744^{mag}$. For comparison, we used two small fractions of the whole field ($image_{small} = 0.15$ x $image_{large}$) for galaxy detection (Figure 2.8). The size of this field ($8.92 \times 10^{-2} deg^2$) is comparable to the Metcalfe data ($9.2 \times 10^{-2} deg^2$) and lies either in a part of the total image where no galaxy overdensity was found (Figure 2.8a) or where the galaxy density is significant above average (Figure 2.8b). Using the same fitting procedure as before, we obtain for:

- large field: zero-point magnitude = 30.72^{mag}

- small field without 'cluster': zero-point magnitude = 30.72^{mag}

- small field with 'cluster'   : zero-point magnitude = 30.97^{mag}

The presence of a galaxy cluster (in a field of size $\sim 8.92 \times 10^{-2} deg^2$) seems to be of importance for the characteristics of the galaxy number count - magnitude relation in such a field (Figure 2.9). However, it is evident that the density of galaxies in the whole field is to high to select a small sub-area for the zero-point calibration.
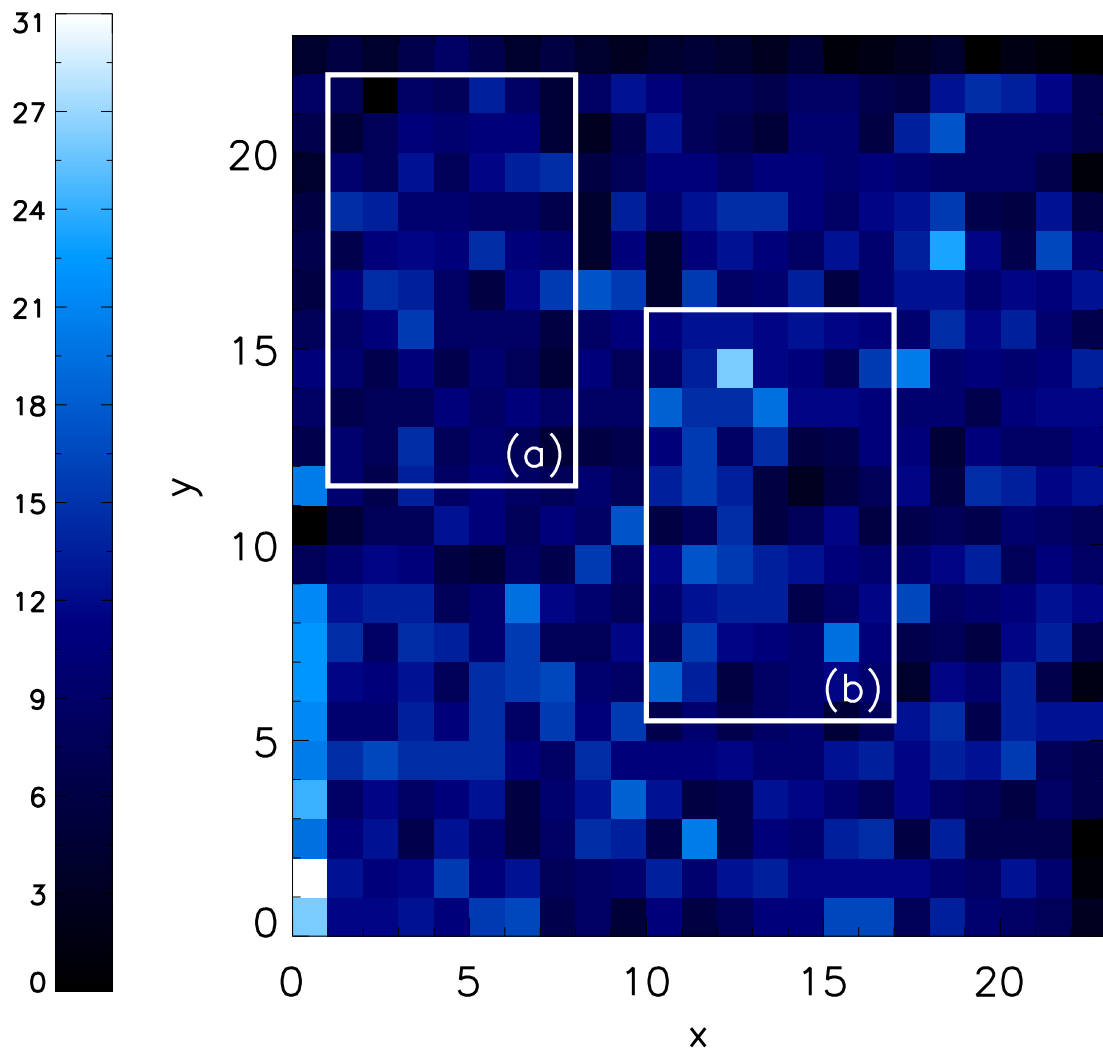
Figure 2.8: The spatial distribution of galaxies in field G030. Galaxies were counted in bins of 100 x 100 pixel. The image shows an overdensity of galaxies above the central bin. The white lines encompass a small sub-areas, which were used to obtain the galaxy number count distributions and zero-point correction in Figure 2.9. Field (a) contains no 'cluster', field (b) does.
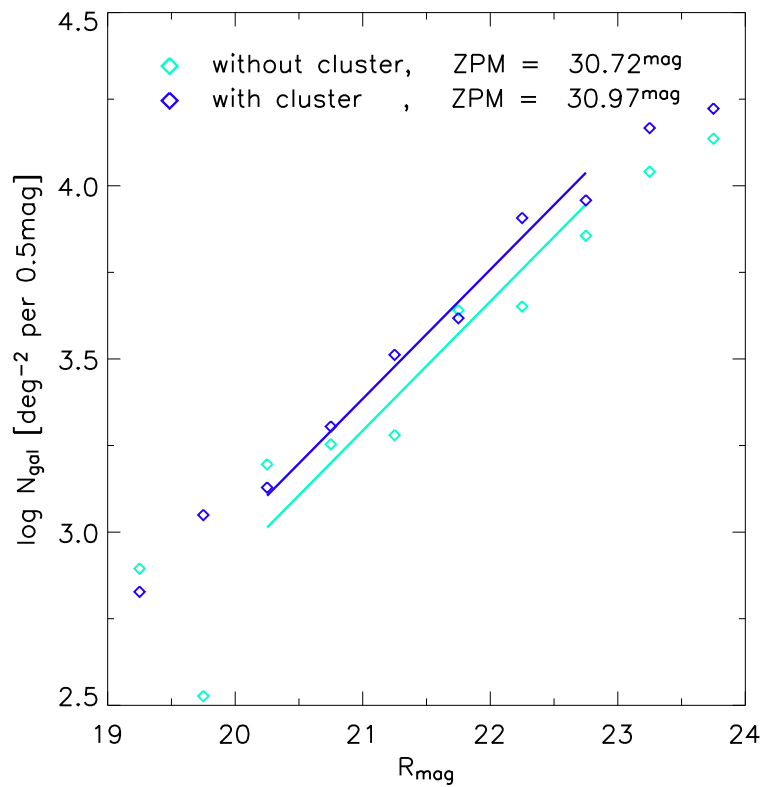
Figure 2.9: Differential galaxy number counts per 0.5 mag interval, normalised to 1deg^2. The lines show the modelled number count-magnitude relation by Metcalfe et al (1991) after correction. The green symbols show the result for a small sub-area, containing no galaxy 'overdensity', the blue symbols the result for same size area containing an 20% larger number of galaxies.

2.1.1.4 Star/Galaxy classification

Although the higher surface density of galaxies with magnitudes of 20≤R≤23 might explain the magnitude offset, we looked for additional parameters able to cause this offset.

The average surface density of galaxies is strongly influenced by the star/galaxy discriminator, which is based on the *stellarity* parameter given by SEXTRACTOR(Bertin and Arnouts 1996). Although a cutoff for the *stellarity* index of ≤0.8 was used to separate galaxies from stars (see section 2.3), I have tested extreme values, e.g. 0.5 and 0.98, for their influence on the zero-point calibration.

The comparison with the result for *stellarity* ≤ 0.8 (see Figure 2.10) shows the $logN_{gal}$ versus R_{mag} relation for three *stellarity* cutoffs. While the *stellarity* index seems to have no impact on the slope of the number count distribution, the calculated zero-point is strongly effected. A higher *stellarity* index results in significant shift of the zero-point towards fainter magnitudes, which would add to an existing zero-point offset. On the other hand, a much lower cutoff affects the zero-point only marginally, approximately 0.1^{mag}, if we use a cutoff ≤ 0.5 instead of ≤ 0.8. Choosing a *stellarity* parameter of ≈ 0.8 restricts its influence on the zero-point calibration well below the offset between R_{CTIO} and R_{SDSS}.

- *stellarity* ≤ 0.5 : zero-point magnitude = 30.64^{mag}

- *stellarity* ≤ 0.8 : zero-point magnitude = 30.74^{mag}

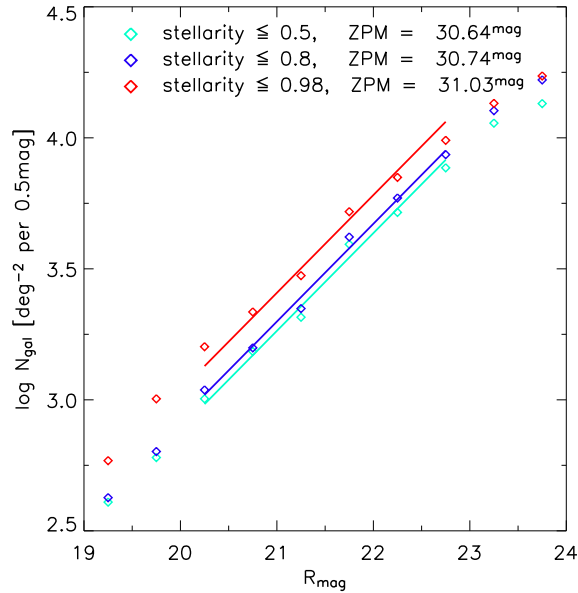- *stellarity* ≤ 0.98 : zero-point magnitude = 31.03^{mag}

Figure 2.10: The star/galaxy separation affects the zero-point, but not the slope of the log N_{gal} vs. R_{mag} distribution. For higher cutoffs, the effect is particularly large. If the stellarity cutoff changes from 0.8 to 0.98 an additional shift of 0.22^{mag} towards fainter magnitudes is observed.

2.1.1.5   Galactic coordinates

Galactic extinction affects both the galaxy number counts and the colours. Our data are not corrected for extinction. Nevertheless, according to de Vaucouleurs and Buta (1983) and references therein, the Sun is at the common apex of two dust-free cones of $\sim 90^o$ aperture centred at the galactic poles. One of their models for galactic extinction assumes A$\equiv$0 at all $|b|>50^o$ (polar windows) and assigns a low value at $|b|< 40^o$, either $A_B = 0.12(|\cos b|-1)$ or $A_B = 0.13(|\cos b|-1)$ (Sandage 1972), with an unspecified smooth transition in the latitude interval $40^o <|b|< 50^o$. The second approximation was successfully used by Chen et al (1999) in their 3-dimensional extinction model. Its application to globular and open cluster data indicates that the COBE/IRAS reddening map by Schlegel et al (1998) has an accuracy of 18% and overestimates visual absorption by a factor of 1.16. This systematic error does not change with galactic latitude.

Carried forward to our survey, we would expect to see no correlation between galaxy number counts (for galaxies with $20 \leq R \leq 23$) or ΔRM and galactic latitudes above $|b| = 50^o$. This is clearly seen in Figures 2.11 and 2.12, which show also no correlation at 'low' galactic latitudes ($|b|< 40^o$) as well.
Although we observe an increase in the surface density of the total galaxy sample at higher galactic latitudes, due to lower incompleteness, there is no correlation between the surface density of faint galaxies and the magnitude offset. That does not allow to draw conclusions regarding the magnitude of extinction as function of galactic latitude. Nevertheless, it eliminates galactic extinction as reason for the zero-point offset.
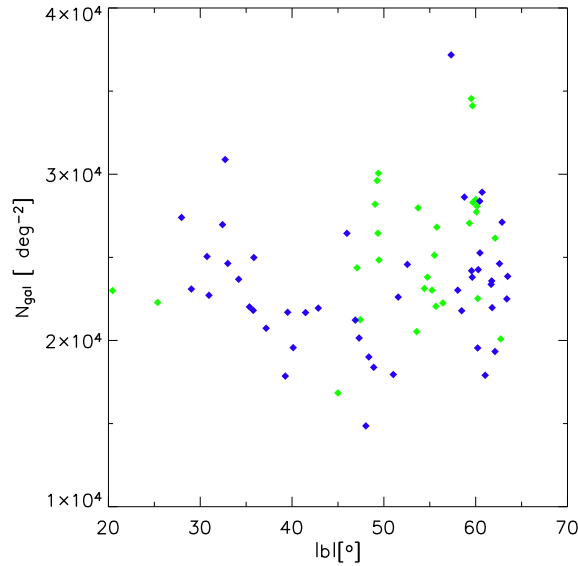

Figure 2.11: The plot of galaxy surface density *vs.* galactic latitude $|b|$ shows no correlation between the two parameters. The blue and green symbols identify galaxies at negative and positive galactic latitudes with $20 \leq R \leq 23$.
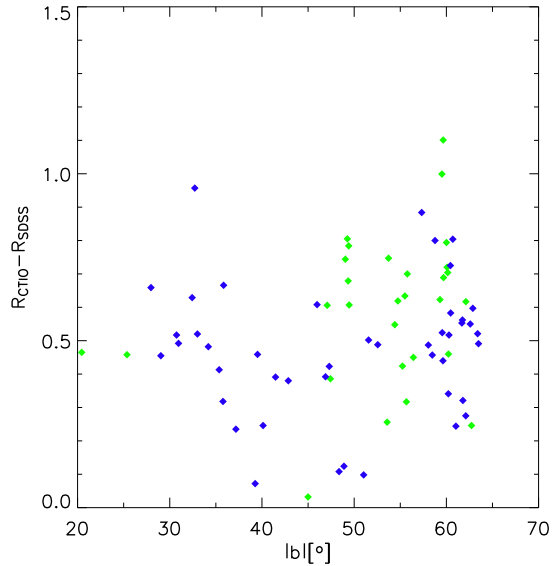
Figure 2.12: The offset in zero-point calibration R_{CTIO}-R_{SDSS} shows no correlation with absolute galactic latitude, either above or below $|b|<40^o$.

   In the previous sections, we have tested different parameters, which may affect the averaged galaxy number density and/or the apparent magnitude. Although there seems to be a correlation between the obtained magnitude offset and the surface density of fainter galaxies, we have no possibility to quantify this effect. Hence, using the calibration derived from the number count-magnitude relation (1991) would results in an imprecise photometry and is therefor not applicable.

Although this is not satisfactory, there are a number of arguments which favour the zero-points derived from the SDSS catalogue. For one, SDSS is calibrated with a large number of stars (N=158). An additional argument comes from the distribution of the zero-points. Theoretically, this distribution would be a delta-function. In reality, we see a distribution with a limited width due to the influence of airmass, extinction etc. Figure 2.13 shows the distribution of zero-points resulting from the number count magnitude relation and after the correction. Additional to a mean offset of 0.52^{mag} (see Figure 2.4), the distribution of the corrected zero-points is much narrower.
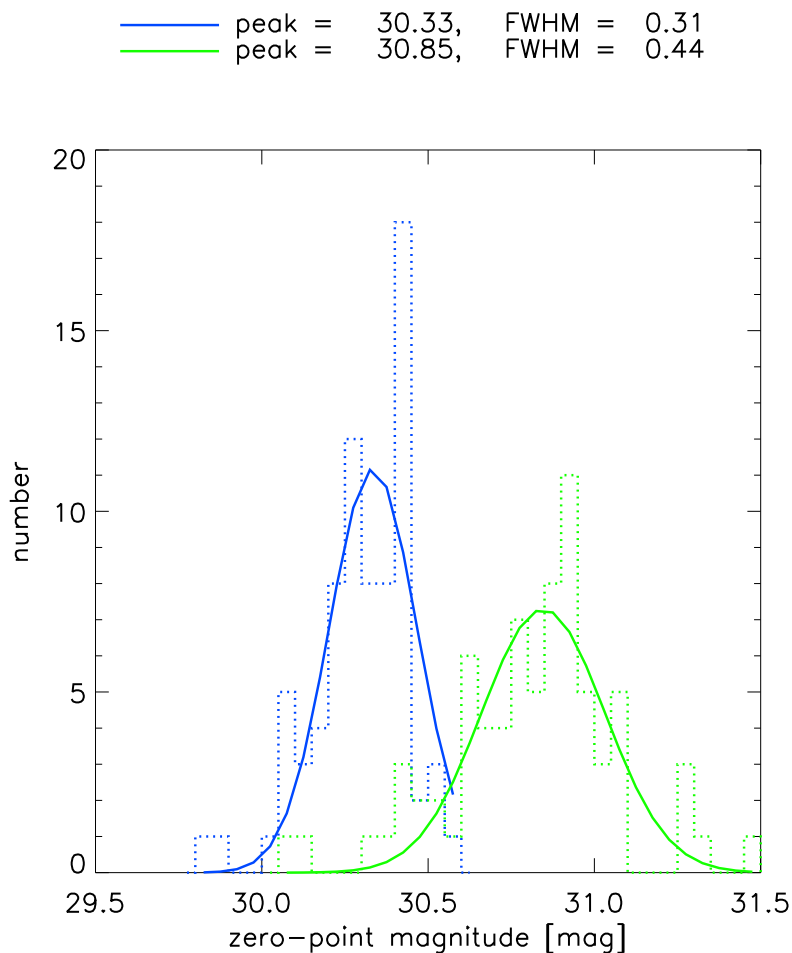

Figure 2.13: Zero-point distribution based on the Metcalfe method (green lines) and from SDSS (blue line).

For comparison we have tested the Metcalfe method on one of our fields, using new R-band data, observed with CAFOS, the **C**alar **A**lto **F**aint **O**bject **S**pectrograph on the 2.2 m telescope on Calar Alto. These data also include standard star observations, and hence allow for a direct comparison between the zero-points.
The magnitude offset derived from eq. 2.2:

- CTIO data - number count distribution: $\Delta RM = 0.689^{mag}$

- CAFOS data - number count distribution: $\Delta RM = 0.660^{mag}$ (Figure 2.14)

also suggest, that there is some systematic error in the number count-magnitude relation.
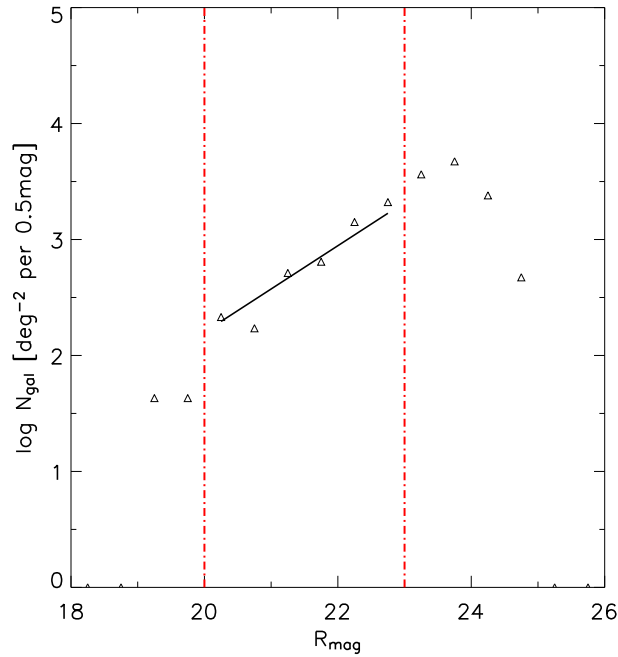

Figure 2.14: Galaxy number count distribution for field G096, observed with CAFOS. From the number count-magnitude relation (eq. 2.2) the zero-point would be at R=23.99^{mag}.

We will not exclude the possibility to use the galaxy number count-magnitude relation as means to calibrate the photometry in a certain band. However, we found this method too sensitive to the average surface density of galaxies in the crucial magnitude range ($20 \leq R \leq 23$). Hence, from this point forward, we use the SDSS photometry of randomly distributed stars in each individual field to calibrate the R-band data.

2.1.2 Detection limit

The total exposure time varies from field to field, since indications for supernova candidates resulted in additional R band observations, and hence longer integration times, for some locations. As a result, the fields differ in depth, which is especially important for assigning a colour to objects which have a near-infrared detection but no optical counter-part. This is the case for many EROs. The application of the detection limit will be described in chapter 2.3. At this point, I will give a short description of how we calculate the detection limit and how it depends on integration time.

Figure 2.15 shows two example fields, with total integration time of 900 and 2040 seconds, respectively. The detection limit is obtained from the $R_{err} vs. R_{mag}$ plot, and corresponds to the maximum R_{mag} for which $R_{err} < 0.1$ magnitudes (R_{err} is the error of the magnitude and given by SEXTRACTOR). Per definition (eq. 2.4) an increase in integration time by a factor 2.2 should result in a detection limit which is approximately 0.9 magnitudes fainter. This fact agrees well with the result in Figure 2.1, $\Delta m = 0.9^{mag}$, going from 900 to 2040 sec integration time.

$$\Delta m = m_1 - m_2 \quad = \quad -2.5 \ log \ \frac{F_{phot,1}}{F_{phot,2}} \qquad (2.4)$$
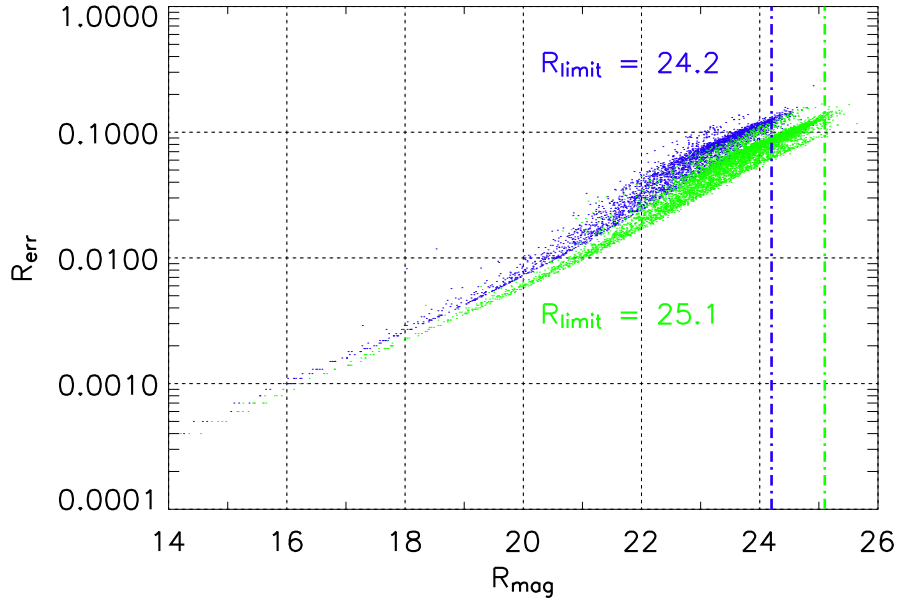

Figure 2.15: The detection limit is given by the magnitude where the majority of objects has photometric errors below 0.1 magnitudes. This value does not coincide with the incompleteness limit, where the number distribution shows a distinct drop-off.

2.2   Near-infrared data

The J-band data were taken during observing runs in October 1997, October 1998 and May 1999 with the 3.5 m telescope on Calar Alto. An additional run in February 2003 was lost due to weather. The observations were carried out using the prime focus camera Omega-Prime (Bizenberger et al. 1998), equipped with a 1024x1024 pixel HAWAII array. The pixel scale of 0.396 arcsec/pixel gave a field of about 6.78 arcmin x 6.78 arcmin. The J band filter λ_C=1.275μm and $\Delta\lambda$= 0.290 μm was used. Each survey field was covered by a mosaic of 4 pointings, each consisting of 4 exposures of 60 seconds with small angular offsets (Herbst et al. 1999). For more details see the upcoming paper by Hempel (2004).

The images were dark- and sky-subtracted using a sky-image constructed from science exposures taken close in time. Each image was then flat-fielded and cosmic rays and bad pixels were removed.

To cover one of the PFCCD images from CTIO, we constructed a 2 x 2 mosaic (see Figure 2.16(a)). The slightly different pixels scale, positional offsets and a different rotation between the R and J-band image was compensated by an alignment of the R-band images.

An example appears in Figure 2.16, indicating regions of varying depth (a). The photometric zero-points were measured using the standard stars from the UKIRT catalogue (Casali and Hawarden 1992) observed at similar airmass as the science data. The effective image quality of the final mosaics ranges from about 1 to 2.1 arcsec in J.
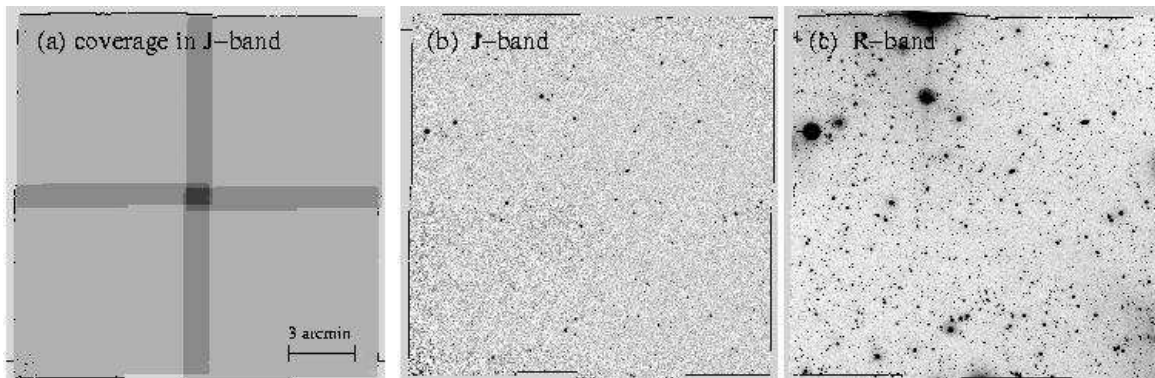

Figure 2.16: Gray-scale image showing the depth of a 2300x2300 pixel J-band mosaic (panel (a)). The brighter regions indicate higher noise due to a smaller number of exposures or bad pixels. The black line encloses the usable region for both J and R-band (panel (b) and (c) respectively).

2.3   Source detection

The J- and R-band magnitudes for the catalogue sources were measured by running SEXTRACTOR2.2.2 (Bertin and Arnouts 1996) in double image mode, in which the J-band image is used to detect the objects and the magnitudes are then measured from the R-band image through the same aperture. Hence, the number of objects is given by the depth of the J-band image. A source must exceed 3σ above the background in at least 5 adjacent pixels.

After compiling a catalogue of red sources, we visually examined each ERO candidate to ensure that it is indeed a real detection (i.e. seen in all exposures, no uncorrected bad pixels, etc.). In a final step, we differentiated between stellar objects and galaxies, both objects with and without optical counterparts.
The colour for objects without R-band detection, i.e. $R \geq R_{limit}$, was calculated in terms of $R_{limit} - J$ instead of $R - J$, making the R-J colour a lower limit. Such objects are marked with an upward arrow in Figure 2.17, which shows the colour magnitude distribution of stellar and non-stellar objects in one field. The details of star-galaxy separation can be found in section 2.3.1.
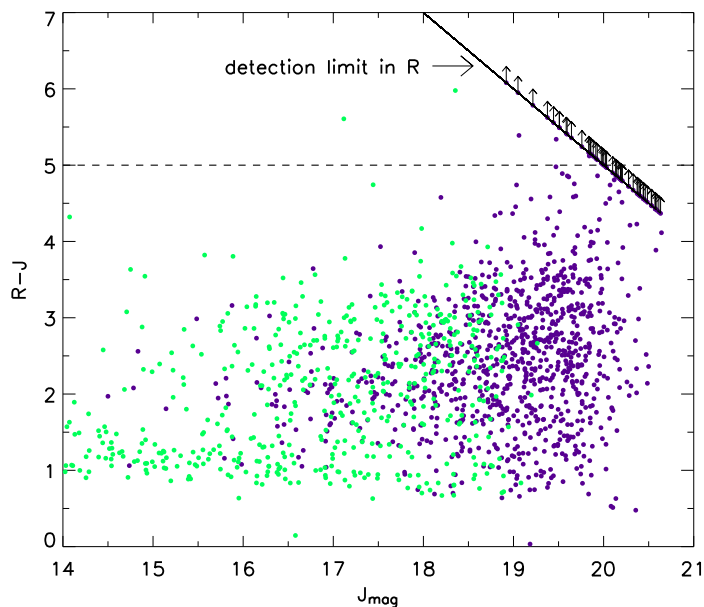

Figure 2.17: Colour-magnitude diagram of a single survey field. Purple symbols show galaxies (*stellarity* ≤ 0.8), green symbols show stars. The majority of the ERO candidates in this field are classified as galaxies. Their calculated R-J colour is a lower limit, either because the source has not been detected in R or its R-band magnitude lies below the detection limit.

2.3.1   Star - Galaxy Separation

Although our selected fields are at relatively high galactic latitude, the frames might contain a small number of stellar objects, which influence the calculation of galaxy number counts especially at faint magnitudes.

There are different principal approaches to the problem of classifying images of astronomical objects into distinct categories, such as stars and galaxies. For our survey we choose a combination of the following criteria:

- photometric limits, i.e. up to which magnitude is an object detectable.

- star-galaxy classifier from SEXTRACTOR (explanation below).

- optical appearance, accepting that galaxy images look more extended or fuzzy than those of stars (or QSOs). In practice, morphological classification is increasingly ambiguous for fainter sources with lower signal-to-noise, and cannot be considered reliable near the limiting magnitude (see also Figure 2.18).

The last criterion was applied only for the classification of ERO candidates, while the general classification of all detected sources relies on the first two criteria.

2.3.2   Stellarity Index

SEXTRACTOR (Bertin and Arnouts 1996) classifies stars and galaxies using the image profile of an object, which is well described by a combination of 8 isophotal areas, the maximum pixel value above the sky and an additional control parameter which is the seeing.
The optical morphologies are thereby classified according to their agreement with a stellar point spread function (PSF), and quantified in the SEXTRACTOR2.2.2 *stellarity* parameter. The value of this parameter ranges from 0.0 for significantly extended sources to 1.0 for those with perfectly stellar PSFs.
For our sample, we divide sources with stellar and galaxy-like counterparts at a *stellarity* $\leq$ 0.8. This value was chosen following the work of Prandoni et al. (1999), Best et al. (2003) and Scodeggio & Silva (2000), who used 0.75, 0.80 and 0.85 respectively.

2.3.3   Detection Limit Tests

To determine the amount of stellar contamination at faint magnitudes, i.e the robustness of the stellarity index, 200 additional objects were randomly placed on a real data frame and extracted in the same way as the final catalogue. We have distinguished between stars, elliptical and spiral galaxies. Figure 2.18 shows the image of a object of each group, detected with SEXTRACTOR2.2.2. These object images have been scaled to magnitudes between 15.25^{mag} and 22^{mag} and added to the original image. This test does not change the angular size of the sources.
Although this procedure adds to the final background around the object, this effect is compensated by SEXTRACTOR by determing and subtracting the mean background at each source position.

Figure 2.19 shows the result of the simulations. In general, the photometry of stars remains very robust over the whole range of magnitudes, and no correction is needed. All stellar objects which have been added to the image were recognised as stars over the whole magnitude range. Therefore, we can exclude a contamination of the galaxy number counts
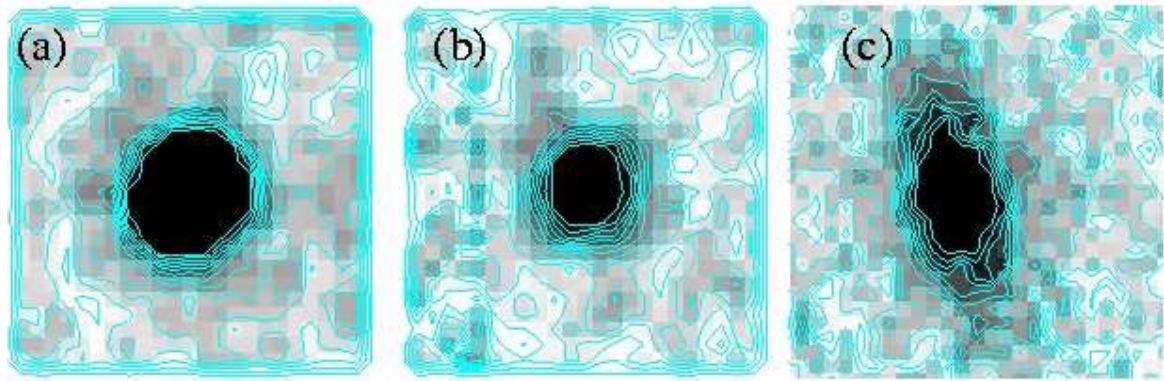
Figure 2.18: The above objects have been used as 'typical' star, elliptical or spiral galaxy for testing brightness limits and accuracy of detecting either object at faint magnitudes. The original J-band magnitude are 15.19^{mag}, 17.48^{mag} 16.32^{mag} for the star, the elliptical and the spiral galaxy respectively. The stellarity index in the original image clearly classifies the star (*stellarity* = 0.98) and the elliptical and spiral galaxy (*stellarity* = 0.02 and 0.01 respectively). The contours are not equally spaced, but visualise the shape of isophots, which are used for the calculation of the *stellarity index*.

by a large number of stars.

The result for galaxies is less promising, as they show a distinct degradation at faint magnitudes. Elliptical and spiral galaxies behave similarly: for faint input magnitudes, the simulated flux is underestimated by up to 0.2^{mag} for ellipticals and 0.5^{mag} for spiral galaxies. On the other hand, all commonly used magnitude-measuring systems suffer biases against low surface brightness objects (Dalcanton 1998), and ours is no exception.

Although the photometric accuracy goes down, the classification as galaxy is as good as for stars. All detected objects are still classified as galaxies.

Note that these simulations were done on one specific field, and while we expect the general behaviour to be similar for all fields, the exact magnitude limits might change with different sky conditions. Some photometric errors may be associated with scaling the brightness, but not the size, of the test targets.
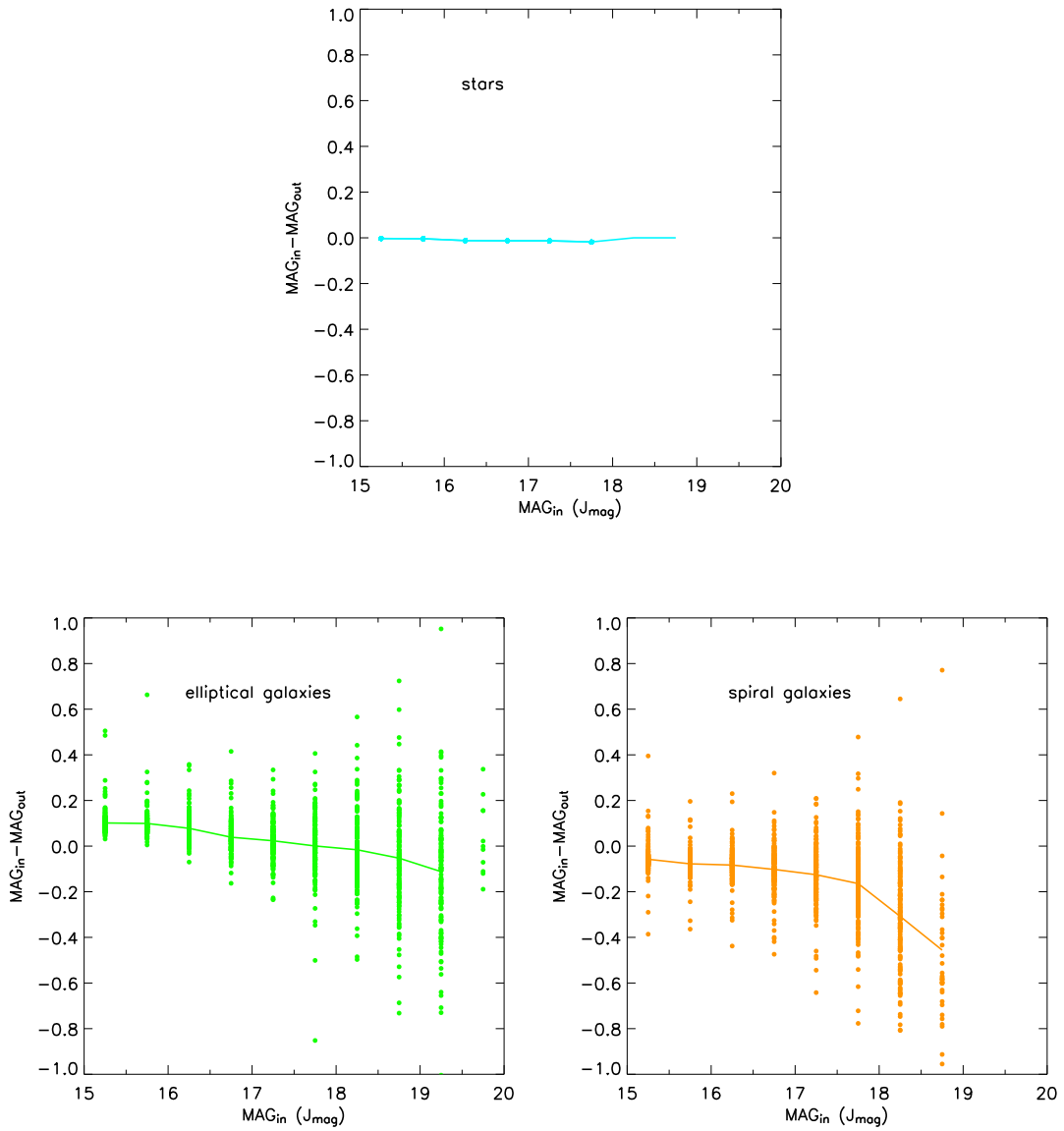
Figure 2.19: Input minus output magnitude for simulated stars, elliptical and spiral galaxies. The lines show the average difference between input magnitude and detected magnitude.